

Homoepitaxy of Crystalline Rubrene Thin Films

Michael A. Fusella¹, Frank Schreiber², Kevin Abbasi³, Jae Joon Kim⁴, Alejandro L. Briseno⁴, and Barry P. Rand^{1,5*}

¹Department of Electrical Engineering, Princeton University, Princeton, NJ 08544 USA.

²Institut für Angewandte Physik, Universität Tübingen, Auf der Morgenstelle 10, 72076 Tübingen, Germany.

³Swagelok Center for Surface Analysis of Materials, Case Western Reserve University, Cleveland, OH 44106 USA.

⁴Polymer Science and Engineering, University of Massachusetts, Amherst, MA 01003 USA.

⁵Andlinger Center for Energy and the Environment, Princeton University, Princeton, NJ 08544 USA.

*Correspondence to: brand@princeton.edu

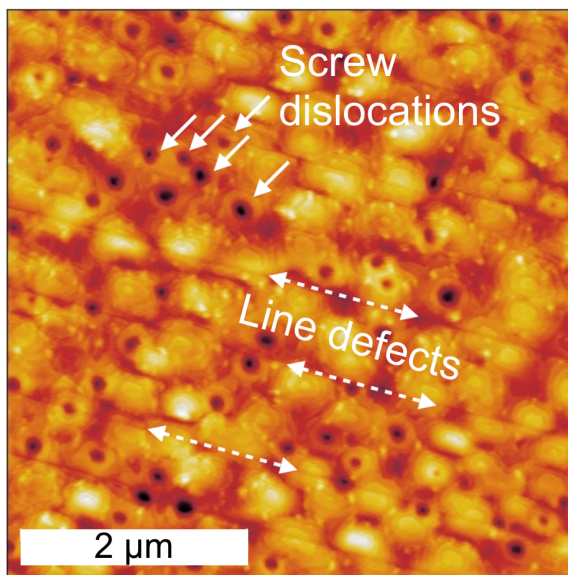
Abstract

We have found that the smooth surface of crystalline rubrene films formed through an abrupt heating process provides a valuable platform to study organic homoepitaxy. By varying growth rate and substrate temperature, we are able to manipulate the onset of a transition from layer-by-layer to island growth modes, while the crystalline thin films maintain a remarkably smooth surface (less than 2.3 nm RMS roughness) even with thick (80 nm) adlayers. We also uncover evidence of point and line defect formation in these films, indicating that homoepitaxy under our conditions is not at equilibrium or strain-free. Point defects that are resolved as screw dislocations can be eliminated under closer-to-equilibrium conditions, whereas we are not able to eliminate the formation of line defects within our experimental constraints at adlayer thicknesses above ~25 nm. We are, however, able to eliminate these line defects by growing on a bulk single crystal of rubrene, indicating that the line defects are a result of strain built into the thin film template. We utilize electron backscatter diffraction – a first for organics – to investigate

the origin of these line defects and find that they preferentially occur parallel to the (002) plane, in agreement with expectations based on calculated surface energies of various rubrene crystal facets. By combining the benefits of crystallinity, low surface roughness, and thickness-tunability, this system provides an important study of attributes valuable to high-performance organic electronic devices.

Keywords: Homoepitaxy, screw dislocation, line defect, roughness, electron backscatter diffraction, crystals, thin films, rubrene

Table of Contents Figure



Electronic devices based on organic thin films promise low-cost fabrication and utilization of flexible substrates.¹ While many devices today feature amorphous films or polycrystalline films with grain sizes on the order of 10-100 nm, organic single crystals have revealed remarkably enhanced optical and electrical properties compared to disordered films. One of the most well-studied molecules in this regard is rubrene, whose orthorhombic polymorph single crystals have demonstrated high mobility (greater than $10 \text{ cm}^2/\text{Vs}$)² and long exciton diffusion lengths of up to $8 \text{ }\mu\text{m}$.³ Despite this, practical device applications require uniform, pinhole-free crystalline thin films, rather than bulk crystals, that can be thickness-tuned to the appropriate device application, thereby necessitating a good understanding of organic thin film epitaxy.^{4,5}

We have previously shown⁶ that as-deposited amorphous rubrene thin films can be transformed into highly crystalline thin films through a heat treatment and, further, that these crystalline films can be thickness-tuned by evaporating additional rubrene on top of the crystal template. In this work we investigate the homoepitaxy of rubrene on top of the crystal template layer as we manipulate growth modes and find evidence of crystal defects. These defects are shown to be a result of either built-in stress or admolecule-flux-driven kinetic effects.⁷ We also successfully employ electron backscatter diffraction (EBSD) – a first for organics – to characterize these thin films. Just as a thorough understanding of epitaxy has proven critical for devices based on III-V inorganic semiconductors, such as GaAs, these results enhance the understanding of organic homoepitaxy in highly crystalline thin films and lay the groundwork to incorporate growth-enhanced performance into the next generation of organic electronic devices. Indeed, compared to III-V materials, crystalline rubrene thin films present a more

practically accessible experimental realm by offering lower processing temperatures (140 °C vs. ~600 °C for GaAs⁸) that are amenable to flexible substrates, and growth under high vacuum conditions rather than the ultra-high vacuum systems necessary for III-V growth via molecular beam epitaxy.

Results and Discussion

We begin by thermally evaporating a ~20 nm film of rubrene onto a thin (5 nm) layer of tris[4-(5-phenylthiophen-2-yl)phenyl]amine (TPTPA, see Fig. 1a inset for molecular structure) atop a glass/ITO substrate. We have found that the amorphous TPTPA underlayer further improves the abrupt-heating-induced crystallization process^{6,9} and allows access to pinhole-free films with remarkably large crystalline domains on the order of hundreds of microns, as seen in the polarized optical microscope (POM) image in Fig. 1a. The rubrene molecules adopt the orthorhombic polymorph ($a = 26.86 \text{ \AA}$, $b = 7.19 \text{ \AA}$, $c = 14.43 \text{ \AA}$) with the (h00) planes parallel to the substrate.^{10,11} A 75 nm thick adlayer grown on top of the crystal template layer enhances contrast in the POM image and single grains retain their uniform color (Fig. 1b). The uniform coloring of each grain suggests that each is a single crystal domain. To prove this, we performed EBSD on three different areas within a single-colored grain for a film like that in Fig. 1b and found the resulting Kikuchi patterns to be identical (Fig. 1c). These results show that homoepitaxy on top of the pristine rubrene crystal propagates the crystal phase and orientation of the underlying crystalline rubrene template layer.

To understand the homoepitaxial adlayer growth at the nano-scale, we employ atomic force microscope (AFM) imaging. We find that the pristine crystal template shown in Fig. 1d exhibits a smooth surface with root mean square (RMS) roughness of

0.77 nm (see Fig. S1 for line scans). Occasionally, however, this smooth surface is interrupted by a molecular step approximately 1.5 nm in size that leads to another smooth terrace (darker red area in Fig. 1d, line scan in Fig. S1). This approximately 1.5 nm molecular step size has been observed repeatedly for rubrene single crystals¹²⁻¹⁶ and is consistent with the (100) layer spacing, $d_{100} = 1.34$ nm. As it has been known for some time that a flat surface is important for improved thin film growth,¹⁷ and therefore the remarkably smooth surface of the crystal template presents an intriguing basis upon which to study epitaxy.

Adlayers ranging from 1 – 80 nm were grown atop the rubrene crystal template layer at a growth rate of 0.1 Å/s and were imaged via AFM. To investigate the effect of substrate temperature, which is known to affect molecular growth modes,¹⁸ we deposited the adlayers at room (20 °C, Fig. 2a-e) and elevated (80 °C, Fig. 2f-j) temperatures (a finer thickness sweep is presented in Figs. S2 and S3, respectively, with line scans presented in Fig. S4). At both temperatures, the 1 nm thick adlayers (Fig. 2a and f) yield a sub-monolayer that is just beginning to coalesce with features approximately 300 nm wide. This scenario would be consistent with layer-by-layer-like growth, as the second monolayer, identified by the few white (higher z-value) areas in Fig. 2a and f, is just starting to form as the first layer is coalescing. The 10 nm adlayer still exhibits layer-by-layer growth for the elevated growth temperature case (Fig. 2g), as another sub-monolayer grows on top of the fully completed growth of previous monolayers. But for the room temperature case, Fig. 2b shows what appears to be the onset of an island growth mode at 10 nm adlayer thickness, as at least two layers are growing on top of a still-incomplete base layer. Moreover, unlike the largely irregularly shaped sub-

monolayer features exhibited in Figs. 2a,f,g, the features in Fig. 2b take on a distinct shape; namely, an elongated hexagon ~ 400 nm wide and ~ 600 nm long. Even at a 25 nm thick adlayer, the elevated temperature case (Fig. 2h) retains a (near-) layer-by-layer growth mode as a single layer grows on top of a layer below that is nearly complete. The room temperature case, however, sees a dramatic new feature appear at 25 nm adlayer thickness (Fig. 2c): Five nearly vertical, parallel “lines” run through the image. These crystallographic line defects, discussed later in more detail, even affect the island growth mode as certain defects “cut through” islands to split them in two. Strikingly, however, though the defect has cut the sample into sections, the growth features remain correlated across the defect, as evidenced by the same molecular step height on either side of the defect. Even growth features influenced by the presence of molecular terraces on the template layer are correlated across these defects (Fig. S5). It should be noted that these line defects do not persist through the entire thickness of the film; rather, the lines begin at a certain adlayer thickness and propagate upwards, with typical depths measured via AFM of approximately 1 – 3 molecular steps.

The line defects and island growth mode persist in the room temperature case throughout the 50 and 80 nm adlayers shown in Figs. 2d and e, respectively. By 80 nm adlayer thickness (Fig. 2e) five molecular steps are common for each island, and a typical island size is about 680 x 920 nm. For the elevated temperature case, the line defects are apparent in the 50 nm and 80 nm adlayer thicknesses (Fig. 2i and j, respectively) and growth has transitioned to an island growth mode with islands averaging 1.4 x 1.9 μm in size. The large difference in island size is an expected result of the variation in growth temperature. At elevated temperatures, an adsorbed molecule can diffuse over much

greater distances before nucleation of a stable island since surface diffusion is a thermally activated process,¹⁹ which correspondingly results in a lower island nucleation density and thus larger island sizes.

A striking result of the growth sequences shown in Fig. 2 is that both growth conditions yield a Stranski-Krastanov growth mode, i.e. layer-by-layer growth that transitions into island growth. Although generally kinetic (non-equilibrium) effects may enter, in a near-equilibrium picture Stranski-Krastanov growth can be seen as arising due to competition between the surface free energy of the deposit, γ_D , the surface free energy of the substrate, γ_S , and the free energy of the interface between the n and $n + 1$ layers, γ_{int} . Following Ref. [19], if $\gamma_S < \gamma_D + \gamma_{int}$ then exposed areas of the substrate are not as energetically costly as exposed areas of deposit and it thus becomes most energetically favorable to form islands that minimize the exposed deposit area and maximize the exposed substrate area. However, if $\gamma_S > \gamma_D + \gamma_{int}$ it then becomes favorable to cover the substrate and grow a complete layer of deposit on top. In general (heteroepitaxy), however, the deposit layer will be strained and will store that elastic energy. As each additional layer is deposited, the strain from the previous layer is incorporated and hence γ_{int} will increase. Thus at some point, the relation $\gamma_S > \gamma_D + \gamma_{int}$ will no longer hold and growth will return to islanding as, again, $\gamma_S < \gamma_D + \gamma_{int}$. The only way to preserve layer-by-layer growth indefinitely is to have $\gamma_S = \gamma_D + \gamma_{int}$ which requires $\gamma_{int} = 0$, a scenario that can only occur in homoepitaxial systems.¹⁹ The fact that Fig. 2 displays Stranski-Krastanov growth features at both temperatures is therefore quite striking for this homoepitaxial system and indicates that, despite perfect lattice matching, a layer growth is still strained as a result of growth not occurring under equilibrium conditions. We note

that the TPTPA underlayer (Fig. S6) is amorphous²⁰ and should therefore not induce lattice strain. Since the onset of islanding and line defects occur at a thicker adlayer for growth at an elevated temperature, this suggests that the additional thermal energy serves to relieve some of this built-in strain but is not able to eliminate it entirely (i.e. $\gamma_{\text{int}, 20^\circ\text{C}} > \gamma_{\text{int}, 80^\circ\text{C}} > 0$). In fact, a similar island growth mode at room temperature and 0.1 Å/s growth rate is seen even for homoepitaxy on rubrene single crystals,²¹ indicating that even a single crystal is not sufficient to avoid the onset of an island growth mode. This may, for instance, be due to a Schwoebel energy barrier.

Another notable result of the growth sequences displayed in Fig. 2 is that even after 80 nm of adlayer growth, the films remain remarkably smooth. To elucidate this, the RMS roughness of the films as a function of adlayer thickness is plotted in Fig. 3. Up to 25 nm adlayer thickness, the values for RMS roughness of the heated (red curve) and room temperature (black curve) growth sequences remain on the same order as a monomolecular step, consistent with a layer-by-layer growth mechanism. Even at the thickest adlayers, however, no significant roughening occurs (in absolute terms), resulting in RMS roughness values of 1.35 and 2 nm for the elevated and room temperature cases, respectively. This can be compared to, for example, the case of a simple kinetic roughening model^{19,22} in which molecules exhibit no inter-layer diffusion, roughness should then approximately scale with the square root of thickness. This model well-describes the growth of certain systems, e.g. PTCDA at room temperature (with an offset of 2 ML).²³ Other systems exhibit more complex scenarios of roughness scaling with thickness, such as the rapid roughening²⁴ and substrate dependent growth²⁵ of diindenoperylene thin films, the interlayer and surface processes intermediate between

colloids and atoms in the case of C₆₀ growth,²⁶ or even the “delayed” roughening mechanism witnessed in amorphous rubrene thin films.²⁷ Considering that many other molecular systems display some form of roughening, in some cases even rapid roughening, it is even more remarkable that for the homoepitaxial growth of crystalline rubrene performed here, the roughness is limited to essentially a monomolecular step. As a numerical comparison, if we had no inter-layer transport, we would expect an additional ~9 nm of RMS roughness for our films, which is an order of magnitude larger than the ~0.6 – 1.2 nm observed. Obviously, there is efficient inter-layer transport (and also intra-layer transport) in our system, which supports the excellent smoothness. We further note that, despite a nominal shift from layer-by-layer to island growth modes, the roughness does not significantly increase, in contrast to conventional growth theory expectations. Though this growth system may be too complicated to be fully explained by traditional growth theory (i.e. kinetic effects, such as a small but finite Schwoebel energy barrier, could account for the slightly increased roughening), the “island” terminology is consistent with what has been previously reported in the literature.²¹

Despite the ability of these films to retain an impressively smooth surface during homoepitaxy, they do not grow defect-free. When the room temperature adlayer growth rate is increased to 1 Å/s, as shown in Fig. 4a, films exhibit the previously mentioned line defects (dashed arrows) as well as “hole” defects (solid arrows). We note that these line and hole defects, as well as the molecular terraces of the islands can even be seen in high-resolution SEM images (Fig. S7). To investigate these hole defects, for rates of 1 Å/s we investigated films of different thickness (Fig. S8) to determine their onset and found that they form when the adlayer is 10 – 15 nm thick (Fig. 4b). These defects typically occur in

the center of a growth island; zooming into one of these islands yields a shallow hole about 4 Å deep (Fig. S9), around which the height increases by approximately one molecular step: the classic description of a screw dislocation. We suspect that these screw dislocations yield a high-energy site in the center of the screw that makes adlayer molecule attachment unfavorable, thereby resulting in a hole as adsorbed molecules that land in this region diffuse across the surface to a more energetically favorable attachment site (for instance, the screw growth front). However, these hole defects can be eliminated simply by decreasing the adlayer growth rate to 0.1 Å/s, as was the case in Fig. 2. To explain this, we propose that at high flux (1 Å/s) the adsorbed molecules diffuse along the surface but are not able to reach the most energetically favorable attachment site before being “trapped in place” by the impinging flux of molecules. This results in a defect around which a screw dislocation forms.

In the context of surface roughness, the screw dislocation holes do not correspond to a smoothly varying surface profile typical for standard analysis of roughness. However, analysis of subsections of the films where no holes are present can be reliably performed and yields an RMS roughness value within ~10% of the value for the whole film (holes included). This, coupled with the fact that the holes do not cover much area naturally (typical hole size 0.012 μm^2 and density 2.88 μm^{-2}), means that their effect on the absolute value of the surface roughness can be neglected. Referring back to Fig. 3, the adlayers grown at 1 Å/s are rougher than their counterparts grown at 0.1 Å/s, though only marginally so, and they again maintain an extremely smooth film even after 80 nm of adlayer growth (RMS roughness of 2.3 nm). Since the holes themselves do not significantly increase the RMS roughness value, it is striking that there is such a distinct

increase in roughness at the adlayer thickness corresponding to the onset of the screw dislocations; this may be due to a simultaneous transition to the island growth mode which results in surface roughening.

The other crystallographic defects seen in Fig. 4a and the thicker adlayers of Fig. 2 are parallel line defects. From our EBSD analysis earlier, we know that each grain in the film is a single crystal domain with the a -axis out-of-plane, but randomly rotated in-plane. Through further analysis of the crystal grains via EBSD, we are able to determine the crystal planes that run parallel to the line defects (Fig. 4c). While each grain has several planes parallel to line defects, every grain was determined to possess line defects that run parallel to the (002) plane. To understand why this is, we estimated the surface energies of the various rubrene crystal facets found in the Bravais, Friedel, Donnay and Harker (BFDH) crystal habit²⁸⁻³⁰ by calculating the intermolecular potentials^{31,32} and following the methods of Refs. [33,34]. The values are given in Table 1, and we find that the lowest surface energy crystal facet is the (200) plane, which is consistent with the experimental fact that this plane has the largest exposed surface area for our thin films (a -axis out of plane) and which is in agreement with observations of bulk rubrene single crystals.³⁵ To understand the line defects, we must first consider that in the case of our epitaxy with built-in strain, the strain will continue to build with each additional monolayer until the energetic cost to expose a new surface is less than the cost to continue storing the ever-increasing elastic energy caused by the growth-induced strain. The first surface to be exposed, then, will be the plane with the next-lowest surface energy as it is, energetically, the least costly to expose. Indeed, we have determined that the (002) facet (10.2 meV/Å²) has the next-lowest surface energy behind the (200) facet

(6.04 meV/Å²). The line defects, which expose new crystal surfaces, will then preferentially occur parallel to the (002) plane, in agreement with our observation that all grains possess line defects running parallel to the (002) plane; this concept is demonstrated schematically in Fig. 4d. Interestingly, the density of these line defects depends on the adlayer growth conditions. Adlayers grown at room temperature and 1 Å/s have the highest line defect density with 1.26 lines/μm (perpendicular to the line defects), as opposed to the relatively similar line defect densities of 0.74 lines/μm and 0.86 lines/μm for 0.1 Å/s adlayers grown at room temperature and 80 °C, respectively. This appears logical, as the high-flux, low-temperature case should be the growth condition furthest from equilibrium; this, in turn, introduces the most strain into the system that can then be relieved by more frequent formation of line defects.

We further investigate these line defects by comparing growth on a rubrene bulk single crystal. Under growth conditions far from equilibrium (1 Å/s and room temperature), we deposit an 80 nm adlayer and find (Fig. 5) that though hole defects are still present (which is expected given this deposition flux, as discussed previously), the line defects are absent. This provides strong evidence that the source of these line defects likely originates from built-in strain between the thin film template layer and growing adlayer. This has substantial implications for the thin film community as it asserts that even a crystalline thin film with a crystallographic phase nominally identical to that of a bulk single crystal could still harbor built-in strain and thus yield quasi-homoepitaxial growth defects.

It could be asserted that the monomolecular steps present on the pristine rubrene crystal template might play a role in the formation of the screw dislocations and line

defects. However, the comparison growth on a rubrene bulk single crystal provides strong evidence that this is not the case. An AFM image of the pristine (no adlayer) rubrene bulk single crystal shows a molecularly smooth surface (Fig. S10). Despite this, adlayer growth on top of the bulk single crystal still yields screw dislocations at high flux (Fig. 5), and the fact that these screw dislocations occur on the thin film template only after 10 – 15 nm adlayer thickness (i.e. approximately 10 monolayers) suggests that the monomolecular steps present on the thin film template surface do not play a significant role in the formation of screw dislocations. Similarly, the line defects were only found to occur after ~25 nm adlayer thickness, by which point, again, the influence of features on the template layer should be small.

Conclusion

We have investigated the homoepitaxy of rubrene on crystalline rubrene thin films and found that, despite near-perfect lattice matching and a polycrystalline template layer wherein each macroscopic grain is a single-crystal domain, a built-in strain exists in this growth system. Though layer-by-layer growth is initially observed for adlayers less than ~10 nm thick, an island growth mode eventually develops with the onset adlayer thickness determined by the growth conditions (flux and temperature). Surface roughness remains remarkably low despite thick adlayer growth and the formation of line and screw defects. Further, we show that the preference of these line defects to occur parallel to the (002) plane is consistent with the surface energies of the various rubrene crystal facets.

These results improve our understanding of epitaxy in organic systems by demonstrating that homoepitaxial growth does not preclude built-in strain. We have also shown that the defects induced by this strain can be entirely eliminated, or have their

onset delayed, by carefully controlling adlayer growth conditions. Further, crystalline thin films may possess built-in strain despite nominally matching the crystal phase of a bulk crystal. Considering the benefits of defect reduction, high crystallinity, low surface roughness, and thickness tunability to high-performance electronic devices, the results of this study underscore the importance of understanding organic semiconductor epitaxial growth.

Methods

All growth was performed on glass substrates pre-patterned with ITO. Substrates were cleaned via successive ultrasonication in deionized water, acetone, and isopropyl alcohol, before receiving an oxygen plasma treatment. Rubrene and TPTPA were purchased from commercial vendors (Nichem and Lumtec, respectively) and were purified via thermal gradient sublimation prior to use. All layers were deposited via thermal evaporation with a base pressure $< 7 \times 10^{-7}$ Torr. TPTPA was evaporated at 0.5 Å/s and rubrene was evaporated as described in the text. To crystallize the template layer, the samples are placed on a pre-heated hotplate set to 140 °C for ~7 minutes in a nitrogen glovebox. Polarized optical microscope images were taken with an Olympus BX60F5, and atomic force microscopy images were taken with a Veeco Innova, model 840-012-711. Intermolecular potential calculations and BFDH morphology were determined using the Mercury software and the crystallographic information file from Ref. 9. We note that while these calculations are not rigorous, our purpose is to compare the relative values of the facet surface energies, instead of asserting the correctness of their absolute values.

A FEI Nova Nanolab 200 FEG-SEM scanning electron microscope was used to image the films at an acceleration voltage of 10 kV and a current of 3.7 nA. The microscope was equipped with an Oxford Nordlys Nano EBSD detector with foreshattered detector diodes to incorporate forward scattered imaging capability. The SEM images presented in this manuscript are all obtained from the foreshatter detectors. Using this, we can combine surface roughness contrast with orientation contrast in a single image. EBSD patterns are acquired from selected regions within the same grain. The registered patterns were then matched with the reference rubrene crystal file to

determine the orientation of the crystal in terms of three Euler angles. The Euler angles were then used to calculate the position of the crystal planes and their orientation.

A FEI Helios Nanolab 650 FEG-SEM equipped with an Elaster XHR immersion lens FESEM column was used to obtain high-resolution images. The UC technology of this column provides a highly focused monochromatic beam stable at an acceleration voltage of 1 kV and a current of 96 pA. This enables us to image the surface features of our samples in high spatial resolution without inducing beam damage. An Elaster in-lens secondary electron detector (TLD-SE) at a reduced working distance of 2 mm was used to improve the signal to noise ratio at intentionally lowered beam conditions.

Rubrene bulk single crystals were grown by the method of horizontal physical vapor transport. Rubrene (Acros Organic) was placed on cleaned glass cylinders as the source for the crystallization and heated to ~ 300 °C. Argon gas with a flow rate of 100 ml min^{-1} was chosen as a carrier gas to prevent oxidization during crystallization. The rubrene crystals used in this study were grown for 5-10 hours.

Supporting Information Available: Figures S1-S9. This material is available free of charge *via* the Internet at <http://pubs.acs.org>.

Acknowledgements

M.A.F. and B.P.R. acknowledge support for this work from the U.S. Department of Energy, Office of Basic Energy Sciences, Division of Materials Sciences and Engineering under Award #DE-SC0012458. J.K. and A.L.B. acknowledge the National Science Foundation (DMR-1508627). F.S. wishes to thank the DFG.

Table 1: Estimated Surface Energies of Various Rubrene Crystal Facets

Crystal Facet	Surface Energy (meV/Å²)
(200)	6.04
(002)	10.2
(111), (11-1), (-11-1), (-111)	13.2

References

1. Forrest, S. R. *Nature* **2004**, *428*, 911–918.
2. Podzorov, V.; Menard, E.; Borissov, A.; Kiryukhin, V.; Rogers, J. A.; Gershenson, M. E. *Phys. Rev. Lett.* **2004**, *93*, 086602.
3. Najafov, H.; Lee, B.; Zhou, Q.; Feldman, L. C.; Podzorov, V. *Nat. Mater.* **2010**, *9*, 938–943.
4. Forrest, S. R. *Chem. Rev.* **1997**, *97*, 1793-1896.
5. Schreiber, F. *Phys. Stat. Sol. (a)* **2004**, *201*, 1037–1054.
6. Verreet, B.; Heremans, P.; Stesmans, A.; Rand, B. P. *Adv. Mater.* **2013**, *25*, 5504–5507.
7. Zhang, Y.; Diao, Y.; Lee, H.; Mirabito, T. J.; Johnson, R. W.; Puodziukynaite, E.; John, J.; Carter, K. R.; Emrick, T.; Mannsfeld, S. C. B.; Briseno, A. L. *Nano Lett.* **2014**, *14* (10), 5547–5554.
8. Miller, J. N.; Low, T. S. *J. Cryst. Growth* **1991**, *111*, 30–38.
9. Lee, H. M.; Moon, H.; Kim, H.-S.; Kim, Y. N.; Choi, S.-M.; Yoo, S.; Cho, S. O. *Org. Electron.* **2011**, *12*, 1446–1453.
10. Jurchescu, O. D.; Meetsma, A.; Palstra, T. T. M. *Acta Cryst.* **2006**, *B62*, 330–334.
11. Reyes-Martinez, M. A.; Crosby, A. J.; Briseno, A. L. *Nat. Commun.* **2015**, *6*, 6948.
12. Hsu, C. H.; Deng, J.; Staddon, C. R.; Beton, P. H. *Appl. Phys. Lett.* **2007**, *91*, 193505.
13. Menard, E.; Marchenko, A.; Podzorov, V.; Gershenson, M. E.; Fichou, D.; Rogers, J. A. *Adv. Mater.* **2006**, *18*, 1552–1556.

14. Mastrogiovanni, D. D. T.; Mayer, J.; Wan, A. S.; Vishnyakov, A.; Neimark, A. V.; Podzorov, V.; Feldman, L. C.; Garfunkel, E. *Sci. Rep.* **2014**, *4*, 4753.
15. Briseno, A. L.; Tseng, R. J.; Ling, M. M.; Falcao, E. H. L.; Yang, Y.; Wudl, F.; Bao, Z. *Adv. Mater.* **2006**, *18*, 2320–2324.
16. Jo, P. S.; Duong, D. T.; Park, J.; Sinclair, R.; Salleo, A. *Chem. Mater.* **2015**, *27*, 3979–3987.
17. Yoshimoto, M.; Maeda, T.; Ohnishi, T.; Koinuma, H.; Ishiyama, O.; Shinohara, M.; Kubo, M.; Miura, R.; Miyamoto, A. *Appl. Phys. Lett.* **1995**, *67*, 2615.
18. Krause, B.; Schreiber, F.; Dosch, H.; Pimpinelli, A.; Seeck, O. H. *Europhys. Lett.* **2007**, *65*, 372–378.
19. Michely, T.; Krug, J. *Islands, Mounds, and Atoms: Patterns and Processes in Crystal Growth Far from Equilibrium*. Springer: Berlin, 2004.
20. Hirade, M.; Adachi, C. *Appl. Phys. Lett.* **2011**, *99* (15), 153302–153304.
21. Zeng, X.; Wang, L.; Duan, L.; Qiu, Y. *Cryst. Growth Des.* **2008**, *8*, 1617–1622.
22. Cohen, P. I.; Petrich, G. S.; Pukite, P. R.; Whaley, G. J.; Arrott, A. S. *Surf. Sci.* **1989**, *216*, 222–248.
23. Fenter, P.; Schreiber, F.; Zhou, L.; Eisenberger, P. *Phys. Rev. B* **1997**, *56*, 3046–3053.
24. Dürr, A. C.; Schreiber, F.; Ritley, K. A.; Kruppa, V.; Krug, J.; Dosch, H.; Struth, B. *Phys. Rev. Lett.* **2003**, *90*, 016104.
25. Kowarik, S.; Gerlach, A.; Sellner, S.; Schreiber, F.; Cavalcanti, L.; Konovalov, O. *Phys. Rev. Lett.* **2006**, *96*, 125504.

26. Bommel, S.; Kleppmann, N.; Weber, C.; Spranger, H.; Schäfer, P.; Novak, J.; Roth, S. V.; Schreiber, F.; Klapp, S. H. L.; Kowarik, S. *Nat. Commun.* **2014**, *5*, 1–8.
27. Kowarik, S.; Gerlach, A.; Sellner, S.; Schreiber, F.; Pflaum, J.; Cavalcanti, L.; Konovalov, O. *Phys. Chem. Chem. Phys.* **2006**, *8*, 1834-1836.
28. Bravais, A. *Études Cristallographiques*. Gauthier Villars: Paris, 1866.
29. Friedel, G. *Bull. Soc. Franc. Mineral.* **1907**, *30*, 326–455.
30. Donnay, J. D. H.; Harker, D. *Am. Mineral.* **1937**, *22*, 463–468.
31. Gavezzotti, A. *Acc. Chem. Res.* **1994**, *27*, 309-314.
32. Gavezzotti, A.; Filippini, G. *J. Phys. Chem.* **1994**, *98*, 4831-4837.
33. Kitaigorodsky, A. I.; Ahmed, N. A. *Acta Cryst.* **1972**, *A28*, 207-210.
34. Verlaak, S.; Steudel, S.; Heremans, P.; Janssen, D.; Deleuze, M. S. *Phys. Rev. B* **2003**, *68*, 195409.
35. Chapman, B. D.; Checco, A.; Pindak, R.; Siegrist, T.; Kloc, C. *J. Cryst. Growth* **2006**, *290*, 479–484.

Figures

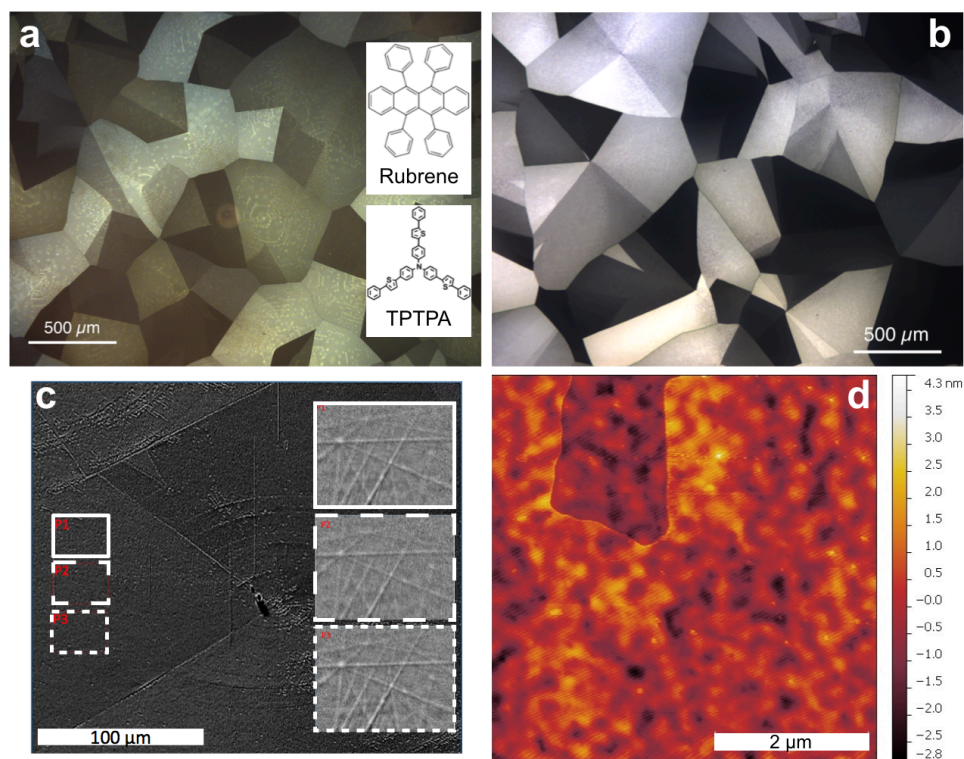


Figure 1. Polarized optical microscope image of (a) a 20 nm thick rubrene crystal template (the molecular structures of rubrene and TPTPA are inset) and (b) the film after 80 nm of adlayer growth showing grains on the order of hundreds of microns that retain their uniform color even after adlayer growth. (c) Scanning electron microscope (SEM) image of the film in (b). Electron backscatter diffraction (EBSD) of three different spots within the same crystal grain reveals identical Kikuchi patterns (insets) thereby proving that each grain is a single crystal domain. (d) Atomic force microscope (AFM) image of the rubrene crystal template in (a) showing a smooth surface interrupted by another smooth surface one molecular step below (darker red region).

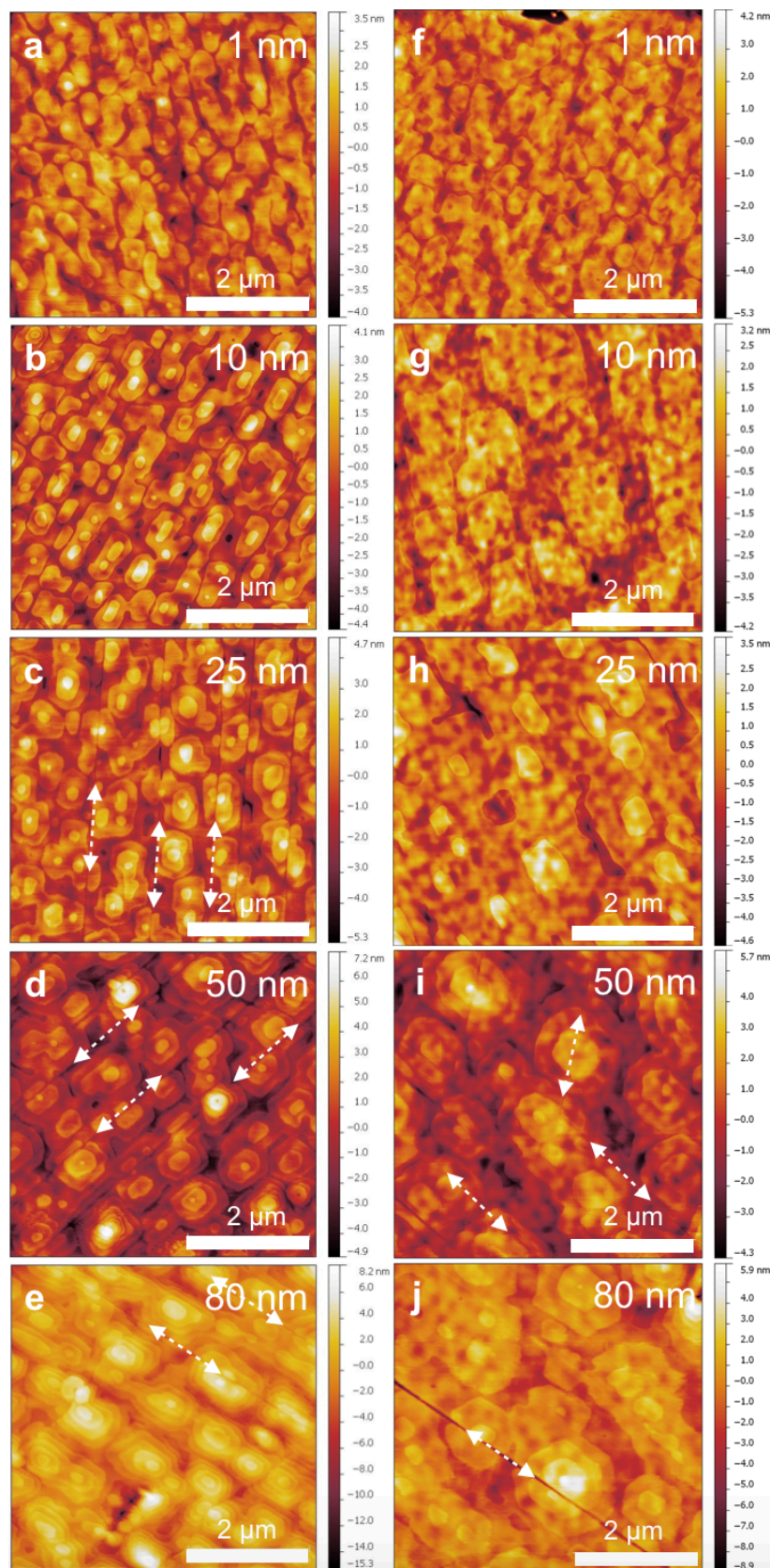


Figure 2. AFM images of varying adlayer thicknesses (identified in image) grown on the rubrene crystal template (a)-(e) at 0.1 Å/s and room temperature substrate or (f)-(j) at 0.1 Å/s and 80 °C substrate temperature. Crystallographic line defects are present in (c), (d), (e), (i), and (j), some of which are emphasized with dashed lines as guides to the eye.

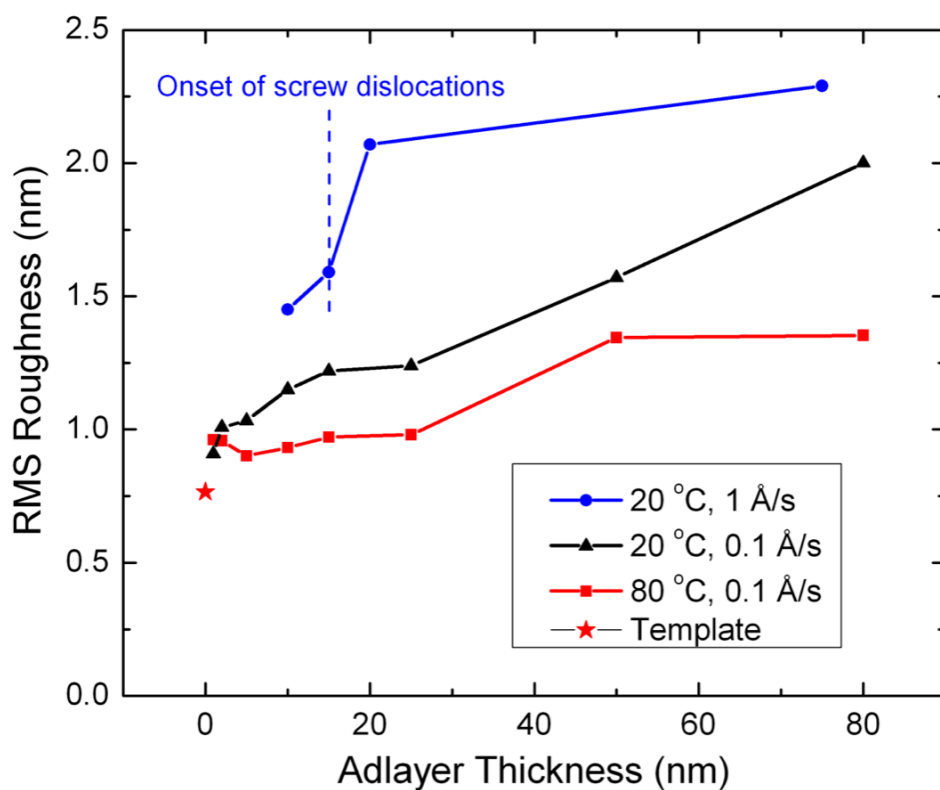


Figure 3. Plot of the root mean square (RMS) roughness as a function of adlayer thickness for growth under various conditions. Though there is some slight variation in RMS roughness between the different growth conditions, all films retain a remarkably smooth surface even when defects are present.

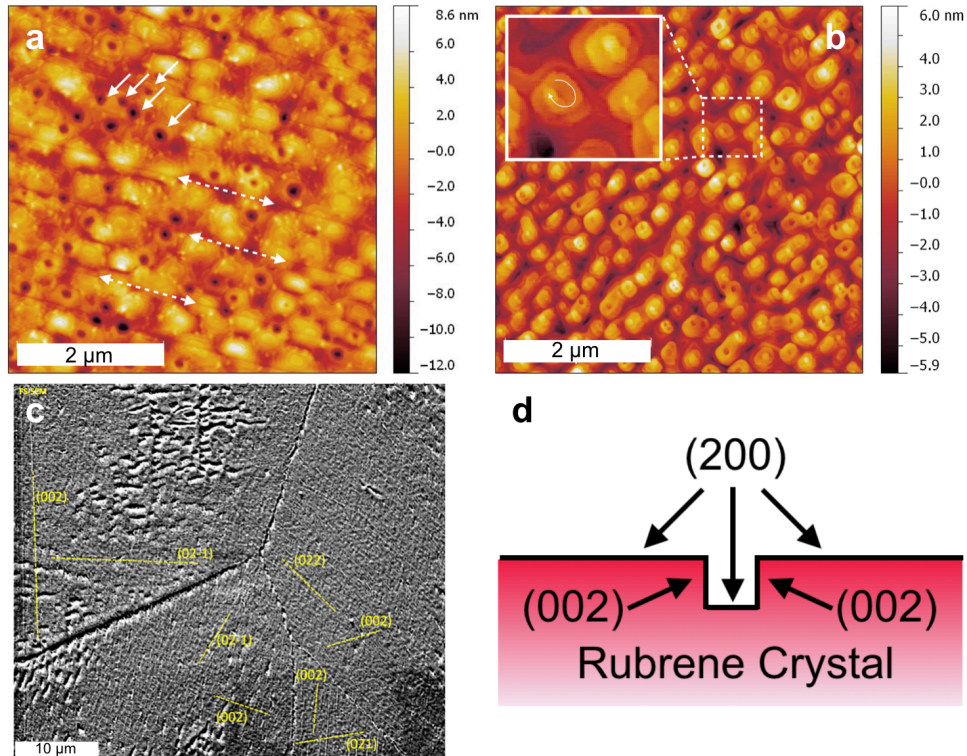


Figure 4. (a) AFM image of an 80 nm adlayer grown at 1 Å/s and room temperature substrate demonstrating “hole” defects (solid arrows) and line defects (dashed arrows). (b) AFM image of 15 nm adlayer grown under the same conditions as (a) showing the onset of screw dislocations with a hole starting to form in the center (inset). (c) SEM image showing line defects in three different grains. EBSD was used to identify (yellow text) the crystal plane parallel to these line defects. (d) Cross-section schematic showing the surfaces exposed when a line defect forms. The (200) plane has the smallest surface energy and thus occupies the largest area. When a line defect exposes a new surface, it most often exposes the plane with the next smallest surface energy, which is the (002) plane.

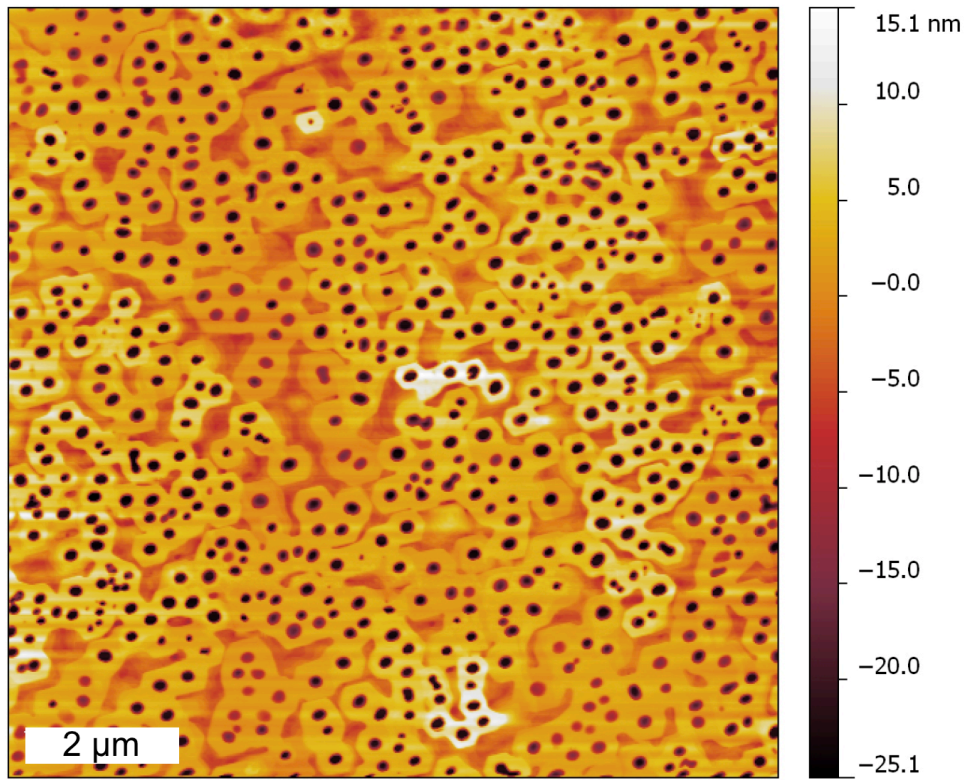


Figure 5. A 10 x 10 μm AFM image of an 80 nm adlayer grown at 1 Å/s and room temperature on a rubrene bulk single crystal showing the presence of hole defects (expected at this flux) but no line defects.